Heatline visualization of natural convection flows within trapezoidal enclosures

E. NATARAJAN
Indian Institute of Technology
Department of Mathematics
Chennai-600036
INDIA

TANMAY BASAK
Indian Institute of Technology
Department of Chemical Engineering
Chennai-600036
INDIA

S. ROY
Indian Institute of Technology
Department of Mathematics
Chennai-600036
INDIA

Abstract: Numerical visualization of heat transport for convective heat transfer were studied by two-dimensional heat function formulation within a trapezoidal cavity, differentially heated in the vertical direction, is presented. Penalty finite element method is used to obtain the isotherm lines, streamlines and heatlines to perceive the understanding of heat and fluid flow. Numerical results are presented for Rayleigh numbers, $Ra = 10^3, 10^6$ and Prandtl numbers, $Pr = 0.7$ and 10. For low Rayleigh number $Ra = 10^3$ it is observed from the heatlines that the heat is transported from the hot wall to the cold wall uniformly. For $Ra = 10^6$ the heat transfer is more intense at the lower-left and upper-right walls of the cavity. Flow characteristics depends strongly on the Rayleigh number and Prandtl number for various side wall inclination angles $\varphi = 45^\circ, 30^\circ$ and 0°. Maximum value of heatline provides directly the value of the average Nusselt number. The secondary circulations were observed for $Ra = 10^6$. Heatlines were observed to predict the energy transfer better than isothermal lines.

Key–Words: penalty finite-element, heatlines, heat transfer, Rayleigh number, inclination angle

1 Introduction

In recent years, an ever-increasing awareness in thermally driven flows reflects that fluid motions and transport processes generated or altered by buoyancy force are of interest due to the practical applications in many fields of science and technology. Consequently, a significant amount of research is being carried out in diverse areas of meteorology, geophysics, energy storage, fire control, studies of air movement in attics and greenhouses, solar distillers, growth of crystals in liquids etc. The essential coupling of transport properties of flow and thermal fields leads to an added complexity in buoyancy driven flows [1]. The majority of works dealing with convection in enclosures is restricted to the cases of simple geometry e.g. rectangular, square, cylindrical and spherical cavities. However, the configurations of actual containers occurring in practice are often far from being simple.

Iyican and Bayazitoglu [2] investigated natural convective flow and heat transfer within a trapezoidal enclosure with parallel cylindrical top and bottom walls at different temperatures and plane adiabatic side walls. The flow features in trapezoidal enclosures are predicted based on data for rectangular enclosures. A critical Rayleigh number is presented depending on the tilting angle, where unicellular convection is observed. Karyakin [3] reported two dimensional laminar natural convection in enclosures of arbitrary cross-section. This study reported on transient natural convection in an isosceles trapezoidal cavity inclined at angle ϕ to the vertical plane and a single circulation region is found in the steady state case. The heat transfer rate is found to increase with the increasing angle in ϕ. Peric [4] studied natural convection in trapezoidal cavities with a series of systematically refined grids from 10×10 to 160×160 and observed the convergence of results for grid independent solutions. Kuyper and Hoogendoorn [5] investigated laminar natural convection flow in trapezoidal enclosures to study the influence of the inclination angle on the flow and also the dependence of the average Nusselt number on the Rayleigh number. Thermosolutal heat transfer within trapezoidal cavity heated at the bottom and cooled at the inclined top part was investigated by Boussaid et al. [6]. The convective heat transport equation was solved by Alternating Direction Implicit(ADI) method combined with a fourth-order compact Hermitian method. Lee [7] studied computational and experimental studies of convective fluid motion within trapezoidal enclosure for differentially heated side walls for aspect ratios of 3 and 6.

Kimura and Bejan [8] proposed heatlines visualization of convective heat transfer through an extension of heat flux line concept to include the advection

terms. The contemporary use of T = constant line is not a proper way to visualize heat transfer in the field of convection. Costa [9] gave a unified viewpoint in both physical and numerical aspects on the treatment of heatlines for visualizing two-dimensional transport problem. It has been applied for natural convection (Bello-Ochende [10], Aggarwal and Manhapra [11], Qi-Hong Deng and Guang-Fa Tang [12],Fu-Yun Zhao et al [13]), boundary layers (Morega and Bejan [14]) and flow in porous media (Morega and Bejan [15]). However heatline visualization were not observed for trapezoidal enclosures. So it is important to study the energy flow using heatlines. The present study deals with natural convection flows within trapezoidal enclosures for differentially heated side walls. The consistent penalty finite element method [16] has been used to solve the nonlinear coupled partial differential equations for flow and temperature fields.

2 Governing equations

Consider a trapezoidal cavity of length L and height H with the left wall inclined at an angle $\varphi = 45^\circ, 30^\circ, 0^\circ$ with Y axis. The velocity boundary conditions are considered as no-slip on solid boundaries. The fluid is considered as incompressible Newtonian and the flow is laminar. For the treatment of the buoyancy term in the momentum equation, Boussinesq approximation is employed to account for the variations of density as a function of temperature, and to couple in this way the temperature field to the flow field. The governing equations after non-dimensionalisation for steady natural convection flow using conservation of mass, momentum and energy can be written as:

$$\frac{\partial U}{\partial X} + \frac{\partial V}{\partial Y} = 0 \tag{1}$$

$$U\frac{\partial U}{\partial X} + V\frac{\partial U}{\partial Y} = -\frac{\partial P}{\partial X} + Pr\left(\frac{\partial^2 U}{\partial X^2} + \frac{\partial^2 U}{\partial Y^2}\right), \tag{2}$$

$$U\frac{\partial V}{\partial X} + V\frac{\partial V}{\partial Y} = -\frac{\partial P}{\partial Y} + Pr\left(\frac{\partial^2 V}{\partial X^2} + \frac{\partial^2 V}{\partial Y^2}\right) + Ra\, Pr\, \theta, \tag{3}$$

$$U\frac{\partial \theta}{\partial X} + V\frac{\partial \theta}{\partial Y} = \frac{\partial^2 \theta}{\partial X^2} + \frac{\partial^2 \theta}{\partial Y^2}, \tag{4}$$

with the boundary conditions (see Fig. 1)

$$\begin{aligned} &U = 0, \quad V = 0, \quad \frac{\partial \theta}{\partial Y} = 0 \qquad \text{on} \quad AB \\ &U = 0, \quad V = 0, \quad \theta = 0 \qquad \text{on} \quad BC \\ &U = 0, \quad V = 0, \quad \theta = 1 \qquad \text{on} \quad AD \\ &U = 0, \quad V = 0, \quad \frac{\partial \theta}{\partial Y} = 0 \qquad \text{on} \quad CD \end{aligned} \tag{5}$$

Here X and Y are dimensionless coordinates varying along horizontal and vertical directions, respectively; U and V are, dimensionless velocity components in the X- and Y-directions, respectively; θ is the dimensionless temperature; P is the dimensionless pressure; Ra and Pr are Rayleigh and Prandtl numbers, respectively.

3 Solution Procedure

The momentum and energy balance equations Eqs. (2-4) are solved using the Galerkin finite element method. The continuity equation (Eq. 1) will be used as a constraint due to mass conservation and this constraint may be used to obtain the pressure distribution [16]. In order to solve Eqs. 2, 3 we use the penalty finite element method where the pressure P is eliminated by a penalty parameter γ and the incompressibility criteria given by Eq. 1 (see Reddy [16]) results in

$$P = -\gamma\left(\frac{\partial U}{\partial X} + \frac{\partial V}{\partial Y}\right). \tag{6}$$

The continuity equation (Eq. 1) is automatically satisfied for large values of γ. Typical values of γ that yield consistent solutions are $10^5 - 10^7$ [16].

Using Eq. (6), the momentum balance equations (Eqs. 2, 3) reduce to

$$U\frac{\partial U}{\partial X} + V\frac{\partial U}{\partial Y} = \gamma\frac{\partial}{\partial X}\left(\frac{\partial U}{\partial X} + \frac{\partial V}{\partial Y}\right) + Pr\left(\frac{\partial^2 U}{\partial X^2} + \frac{\partial^2 U}{\partial Y^2}\right), \tag{7}$$

and

$$U\frac{\partial V}{\partial X} + V\frac{\partial V}{\partial Y} = \gamma\frac{\partial}{\partial Y}\left(\frac{\partial U}{\partial X} + \frac{\partial V}{\partial Y}\right) + Pr\left(\frac{\partial^2 V}{\partial X^2} + \frac{\partial^2 V}{\partial Y^2}\right) + Ra\, Pr\, \theta \tag{8}$$

Expanding the velocity components $(U,\ V)$ and temperature (θ) using basis set $\{\Phi_k\}_{k=1}^N$ as,

$$U \approx \sum_{k=1}^{N} U_k\, \Phi_k(X,Y), \quad V \approx \sum_{k=1}^{N} V_k\, \Phi_k(X,Y), \quad \text{and} \quad \theta \approx \sum_{k=1}^{N} \theta_k\, \Phi_k(X,Y), \tag{9}$$

the Galerkin finite element method yields the following nonlinear residual equations for Eqs. (7), (8) and (4), respectively, at nodes of internal domain

Ω:

$$R_i^{(1)} = \sum_{k=1}^{N} U_k \int_\Omega \left[\left(\sum_{k=1}^{N} U_k \Phi_k \right) \frac{\partial \Phi_k}{\partial X} + \left(\sum_{k=1}^{N} V_k \Phi_k \right) \frac{\partial \Phi_k}{\partial Y} \right] \Phi_i dX dY + \gamma \left[\sum_{k=1}^{N} U_k \int_\Omega \frac{\partial \Phi_i}{\partial X} \frac{\partial \Phi_k}{\partial X} \, dX dY \right] + \gamma \left[\sum_{k=1}^{N} V_k \int_\Omega \frac{\partial \Phi_i}{\partial X} \frac{\partial \Phi_k}{\partial Y} \, dX dY \right] + Pr \sum_{k=1}^{N} U_k \int_\Omega \left[\frac{\partial \Phi_i}{\partial X} \frac{\partial \Phi_k}{\partial X} + \frac{\partial \Phi_i}{\partial Y} \frac{\partial \Phi_k}{\partial Y} \right] dX dY \quad (10)$$

$$R_i^{(2)} = \sum_{k=1}^{N} V_k \int_\Omega \left[\left(\sum_{k=1}^{N} U_k \Phi_k \right) \frac{\partial \Phi_k}{\partial X} + \left(\sum_{k=1}^{N} V_k \Phi_k \right) \frac{\partial \Phi_k}{\partial Y} \right] \Phi_i dX dY + \gamma \left[\sum_{k=1}^{N} U_k \int_\Omega \frac{\partial \Phi_i}{\partial Y} \frac{\partial \Phi_k}{\partial X} \, dX dY \right] + \gamma \left[\sum_{k=1}^{N} V_k \int_\Omega \frac{\partial \Phi_i}{\partial Y} \frac{\partial \Phi_k}{\partial Y} \, dX dY \right] + Pr \sum_{k=1}^{N} V_k \int_\Omega \left[\frac{\partial \Phi_i}{\partial X} \frac{\partial \Phi_k}{\partial X} + \frac{\partial \Phi_i}{\partial Y} \frac{\partial \Phi_k}{\partial Y} \right] dX dY - RaPr \int_\Omega \left(\sum_{k=1}^{N} \theta_k \Phi_k \right) \Phi_i \, dX dY \quad (11)$$

and

$$R_i^{(3)} = \sum_{k=1}^{N} \theta_k \int_\Omega \left[\left(\sum_{k=1}^{N} U_k \Phi_k \right) \frac{\partial \Phi_k}{\partial X} + \left(\sum_{k=1}^{N} V_k \Phi_k \right) \frac{\partial \Phi_k}{\partial Y} \right] \Phi_i \, dX dY + \sum_{k=1}^{N} \theta_k \int_\Omega \left[\frac{\partial \Phi_i}{\partial X} \frac{\partial \Phi_k}{\partial X} + \frac{\partial \Phi_i}{\partial Y} \frac{\partial \Phi_k}{\partial Y} \right] dX dY. \quad (12)$$

The non-linear residual equations (Eqs. 10-12) are solved using a Newton-Raphson procedure to determine the coefficients of the expansions in Eq. (9). At each iteration, the linear $(3N \times 3N)$ system;

$$\mathbf{J}\left(\mathbf{a}^n\right)\left[\mathbf{a}^n - \mathbf{a}^{n+1}\right] = \mathbf{R}\left(\mathbf{a}^n\right) \ , \quad (13)$$

is solved where n is the iterative index. The elements of the Jacobian matrix, $\mathbf{J}(\mathbf{a}^n)$ contain the derivatives of the residual equations with respect to velocity components (U_j)'s, (V_j)'s and the temperature (θ_j's) and $\mathbf{R}(\mathbf{a}^n)$ is the vector of residuals. The linear system for each iteration is based on efficient node numbering of the elements such that the jacobian forms a banded matrix. The iterative process is terminated with the convergence criterion $\left[\sum \left(R_i^{(j)}\right)^2\right]^{0.5} \leq 10^{-5}$ using two-norm of residual vectors.

We have used nine node bi-quadratic elements with each element mapped using iso-parametric mapping [16] from $X-Y$ to a unit square $\xi-\eta$ domain as illustrated in Fig. 9. Subsequently, the domain integrals in the residual equations are evaluated using nine node bi-quadratic basis functions in $\xi-\eta$ domain as:

$$X = \sum_{i=1}^{9} X_i \Phi_i(\xi,\eta) \quad \text{and} \quad Y = \sum_{i=1}^{9} Y_i \Phi_i(\xi,\eta) \ , \quad (14)$$

where $\Phi_i(\xi,\eta)$ are the local bi-quadratic basis functions on the $\xi-\eta$ domain. The integrals in Eqs. (10)-(12) can be evaluated in $\xi-\eta$ domain using following relationships:

$$\begin{bmatrix} \frac{\partial \Phi_i}{\partial X} \\ \frac{\partial \Phi_i}{\partial Y} \end{bmatrix} = \frac{1}{J} \begin{bmatrix} \frac{\partial Y}{\partial \eta} & -\frac{\partial Y}{\partial \xi} \\ -\frac{\partial X}{\partial \eta} & \frac{\partial X}{\partial \xi} \end{bmatrix} \begin{bmatrix} \frac{\partial \Phi_i}{\partial \xi} \\ \frac{\partial \Phi_i}{\partial \eta} \end{bmatrix}$$

and

$$dX dY = J d\xi d\eta \quad (15)$$

where

$$J = \frac{\partial(X,Y)}{\partial(\xi,\eta)} = \begin{vmatrix} \frac{\partial X}{\partial \xi} & \frac{\partial X}{\partial \eta} \\ \frac{\partial Y}{\partial \xi} & \frac{\partial Y}{\partial \eta} \end{vmatrix} .$$

4 Evaluation of Heat function and Stream function

4.1 Heat function

Energy equation in non-dimensional form can be written as,

$$\frac{\partial}{\partial X}(U\theta - \frac{\partial \theta}{\partial X}) + \frac{\partial}{\partial X}(V\theta - \frac{\partial \theta}{\partial Y}) = 0$$

which gives

$$\frac{\partial H}{\partial Y} = U\theta - \frac{\partial \theta}{\partial X} \quad (16)$$

$$-\frac{\partial H}{\partial X} = V\theta - \frac{\partial \theta}{\partial Y} \quad (17)$$

H = H(X,Y) is the heat function. Heat can be considered to flow along constant H lines, which, in analogy to streamlines, are called heatlines.

Differentiating Eq. (16) and (17) w.r.t Y and X and adding gives

$$\frac{\partial^2 H}{\partial X^2} + \frac{\partial^2 H}{\partial Y^2} = \frac{\partial}{\partial Y}(U\theta) - \frac{\partial}{\partial X}(V\theta) \qquad (18)$$

Expanding the heat function (H) using basis set $\{\Phi_k\}_{k=1}^{N}$ as,

$$H \approx \sum_{k=1}^{N} H_k \, \Phi_k(X,Y) \qquad (19)$$

the Galerkin finite element method yields the following residual equation for Eq. (18)

$$\begin{aligned} R_i^s &= \sum_{k=1}^{N} H_k \int_\Omega \left[\frac{\partial \Phi_i}{\partial X}\frac{\partial \Phi_k}{\partial X} + \frac{\partial \Phi_i}{\partial Y}\frac{\partial \Phi_k}{\partial Y}\right] dXdY \\ &+ \sum_{k=1}^{n}\sum_{l=1}^{n} U_k\theta_l \int_\Omega (\Phi_l \frac{\partial \Phi_k}{\partial Y} + \Phi_k \frac{\partial \Phi_l}{\partial Y})\Phi_i dXdY \\ &- \sum_{k=1}^{n}\sum_{l=1}^{n} V_k\theta_l \int_\Omega (\Phi_l \frac{\partial \Phi_k}{\partial X} + \Phi_k \frac{\partial \Phi_l}{\partial X})\Phi_i dXdY \end{aligned} \qquad (20)$$

The boundary conditions on H follow from the definition of heat function, Eq.(16) and (17):

$$H = \int_0^s (cos\varphi \frac{\partial \theta}{\partial X} + sin\varphi \frac{\partial \theta}{\partial Y}) ds_1 \;\text{ on }\; AD$$

$$H = \int_0^s (cos\varphi \frac{\partial \theta}{\partial X} - sin\varphi \frac{\partial \theta}{\partial Y}) ds_2 \;\text{ on }\; BC$$

$$H = 0 \;\text{ on }\; AB \;\text{ and }\; H = \overline{Nu_h} \;\text{ on }\; CD \qquad (21)$$

where ds_1 and ds_2 are the small elemental lengths along the left and right walls and $\varphi = 45°, 30°, 0°$.

4.2 Stream function

The fluid motion is displayed using the stream function ψ obtained from velocity components U and V. The relationships between stream function, ψ (see Batchelor [17]) and velocity components for two dimensional flows are

$$U = \frac{\partial \psi}{\partial Y}\,, \quad V = -\frac{\partial \psi}{\partial X}\,, \qquad (22)$$

which yield a single equation

$$\frac{\partial^2 \psi}{\partial X^2} + \frac{\partial^2 \psi}{\partial Y^2} = \frac{\partial U}{\partial Y} - \frac{\partial V}{\partial X}\,. \qquad (23)$$

Using the above definition of the stream function, the positive sign of ψ denotes anti-clockwise circulation and the clockwise circulation is represented by the negative sign of ψ. Expanding the stream function (ψ) using the basis set $\{\Phi\}$ as $\psi = \sum_{k=1}^{N} \psi_k \Phi_k(X,Y)$ and the relation for U , V from Eq. (9), the Galerkin finite element method yield the following linear residual equations for Eq. (23).

$$\begin{aligned} R_i^s &= \sum_{k=1}^{N} \psi_k \int_\Omega \left[\frac{\partial \Phi_i}{\partial X}\frac{\partial \Phi_k}{\partial X} + \frac{\partial \Phi_i}{\partial Y}\frac{\partial \Phi_k}{\partial Y}\right] dXdY \\ &+ \sum_{k=1}^{n} U_k \int_\Omega \Phi_i \frac{\partial \Phi_k}{\partial Y} dXdY \\ &- \sum_{k=1}^{n} V_k \int_\Omega \Phi_i \frac{\partial \Phi_k}{\partial X} dXdY \end{aligned} \qquad (24)$$

The no-slip condition is valid at all boundaries as there is no cross flow, hence $\psi = 0$ is used as residual equations at the nodes for the boundaries. The bi-quadratic basis function is used to evaluate the integrals in Eq. (24) and ψ's are obtained by solving the N linear residual equations

5 Numerical tests

Numerically there are primarily two methods to solve the incompressible fluid flow: (i) vorticity-based method (ii) primitive variable method

The disadvantage of vorticity method is, the difficulty in specifying value of the vorticity which is often the cause of trouble in getting a converged solution. Therefore, primitive variable i.e, pressure velocity method is applied broader and adopted in the present study. In penalty finite element method the incompressibility constraint and pressure are related through the addition of a penalized parameter into the Galerkin formulation. The computational domain consists of 20 $\times$ 20 bi-quadratic elements which correspond to 41 $\times$ 41 grid points in ξ-η domain as seen in Fig. 9. To ensure the convergence of the numerical solution to the exact solution, the grid sizes have been optimized and the results presented here are independent of grid sizes.

6 Results and discussion

Flow patterns were discussed for various side wall inclination angles $\varphi = 45°, 30°, 0°$ for $Pr = 0.7$ and 10. In Fig. 2, for $Ra = 10^3$, $Pr = 0.7$ the flow intensity is very low and heat transfer occurs mainly due to conduction. Streamlines are of clockwise unicellular flow structure, with low values such as $\psi_{min} = -1.1$ indicating the weak convection. The heat transfer is mainly dominated by conduction, isotherms exhibit pseudo-conduction structure. It is observed from the heatlines that the heat is transported from the hot wall to the cold wall uniformly. The heat transfer is more intense at the lower-left and upper-right walls of the cavity. It is observed that isothermal lines are poorer to visualize the heat transfer as seen in Fig. 3. The maximum value of the heatline provides directly the value of the average Nusselt number. The positive values of lines refer to the heat transfer from hot wall to cold wall whereas negative value implies eddies. For $Ra = 10^6$ the convection is strengthened, as indicated by minimum value of streamlines $\psi_{min} = -20$ which gets broken into two secondary circulation. The effect of convection is more pronounced in the isotherm patterns also. Similarly, for $\varphi = 30°, 0°$ the streamline with $\psi = -18, -16.5$ develops more secondary circulations (Figs. 3, 5, 7) indicating stronger convection for $\varphi = 45°$ compared to $\varphi = 30°$ and $0°$ (square). For $Ra = 10^6$ the heatlines crossing the hot wall are more crowded near the bottom side than those near the top side. This shows the non-uniform distribution of the heat flux over the walls. For $Pr = 0.7$ the heatline with $H = -7$ for $\varphi = 45°$ circulate as a core (Fig. 3) emphasizing the importance of conduction. This core gets reduced in size and moved towards the hot wall for $\varphi = 30°$ (Fig. 5) and disappears for $\varphi = 0°$ (Fig. 7) because of increase in the convection.

When the Prandtl number is increased from 0.7 to 10 the streamlines strength increases due to increased convection. For $Pr = 0.7$ the heatline with $H = -7$ for $\varphi = 45°, 30°$ becomes a stronger circulation, expanded and moved towards the cold wall for $Pr = 10$ (Figs. 3, 4, 5, 6). For $\varphi = 0°$ (square) the vertical heatline boundary layer thickness increases for $Pr = 10$ compared to $Pr = 0.7$ due to low thermal conductivity (Figs. 7, 8).

7 Conclusion

In this paper, the method of using heat functions to visualize the heat transport for convective heat transfer within trapezoidal enclosure has been analysed. The following conclusions can be obtained:

- The functions defined based on dimensionless variables are more general and straightforward than that in dimensional form.
- Heatlines are the best way to visualize net flow of heat energy than isothermal lines.
- Effect of side wall inclination angle of the trapezoidal cavity is more pronounced in the heat transfer.
- Dependence of flow characteristics on Rayleigh number and Prandtl number becomes prominent.

References:

[1] A. Bejan, *Convection heat transfer,* 3rd ed., Wiley, New York 2004.

[2] L. Iyican, Y. Bayazitoglu, An Analytical Study of Natural Convective Heat Transfer within Trapezoidal Enclosure, *ASME Tans. J. Heat Transfer.* 102, 1980, pp. 640–647.

[3] YU. E. Karyakin, Transient natural convection in prismatic enclosures of arbitrary cross-section, *Int. J. Heat Mass Transfer.* 32, 1989, pp. 1095–1103.

[4] M. Perić, Natural convection in trapezoidal cavities, *Numer. Heat Transfer Part A.* 24, 1993, pp. 213–219.

[5] R. A. Kuyper, C. J. Hoogendoorn, Laminar Natural convection flow in trapezoidal enclosures, *Numer. Heat Transfer Part A.* 28, 1995, pp. 55–67.

[6] M. Boussaid, A. Djerrada, M. Bouhadef, Thermosolutal transfer within trapezoidal cavity, *Numer. Heat Transfer Part A.* 43, 2003, pp. 431–448.

[7] T. S. Lee, Computational and experimental studies of convective fluid motion and heat transfer in inclined non-rectangular enclosures, *Int. J. Heat Fluid flow.* 5, 1984, pp. 29–36.

[8] S. Kimura and A. Bejan, The Heatline Visualization of convective Heat transfer, *ASME Trans. J Heat Transfer.* 105, 1983, pp. 916–919.

[9] V. A. F. Costa, Unification of the streamline, heatline and massline methods for the visualization of two-dimensional transport phenomena, *Int. J. Heat Mass Transfer.* 42, 1999, pp. 27–33.

[10] F. L. Bello-Ochende, A Heat function formulation for thermal convection in a square cavity, *Int. Comm. Heat Transfer.* 15, 1988, pp. 193–202.

[11] S. K. Aggarwal, A. Manhapra, Use of heatlines for unsteady buoyancy-driven flow in a cylindrical enclosure, *ASME Trans. J Heat Transfer.* 111, 1989, pp. 576–578.

[12] Qi-Hong Deng, Guang-Fa Tang, Numerical visualization of mass and heat transport for conjugate natural convection/heat conduction by streamline and heatline, *Int. J. Heat Mass Transfer.* 45, 2002, pp. 2373–2385.

[13] Fu-Yun Zhao, Di Liu, Guang-Fa Tang, Application issues of the streamline, heatline and massline for conjugate heat and mass transfer, *Int. J. Heat Mass Transfer.* 50, 2007, pp. 320–334.

[14] M. Morega, A. Bejan, Heatline visualization of forced convection laminar boundary layers, *Int. J. Heat Mass Transfer.* 36, 1993, pp 3957–3966.

[15] M. Morega, A. Bejan, Heatline visualization of forced convection in porous media, *Int. J. Heat Fluid Flow.* 36, 1994, pp 42–47.

[16] J. N. Reddy , *An Introduction to the Finite Element Method,* McGraw–Hill, New York 1993.

[17] G. K. Batchelor, *An Introduction to Fluid Dynamics,* Cambridge University Press, 1993.

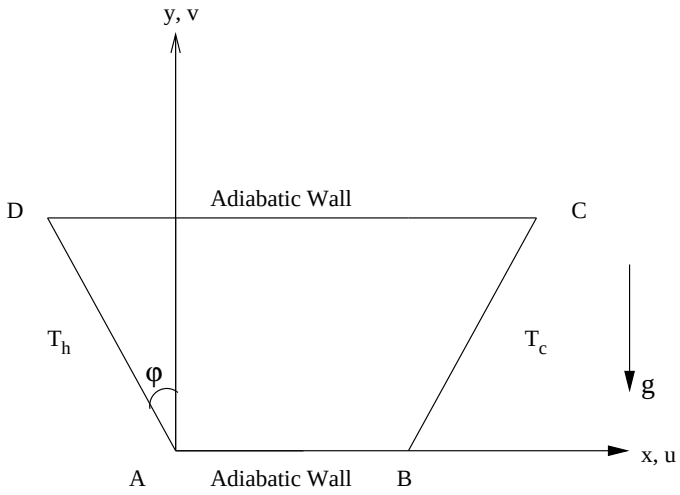

Figure 1: Schematic diagram of the physical system.

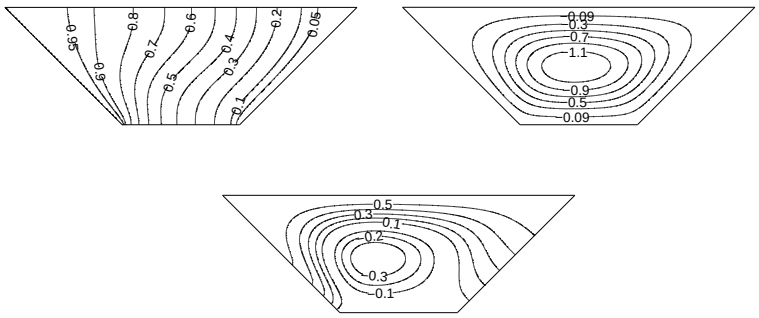

Figure 2: Temperature (left), stream function (right) and heatlines (bottom) for $Ra = 10^3$ and $Pr = 0.7$ with $\varphi = 45°$.

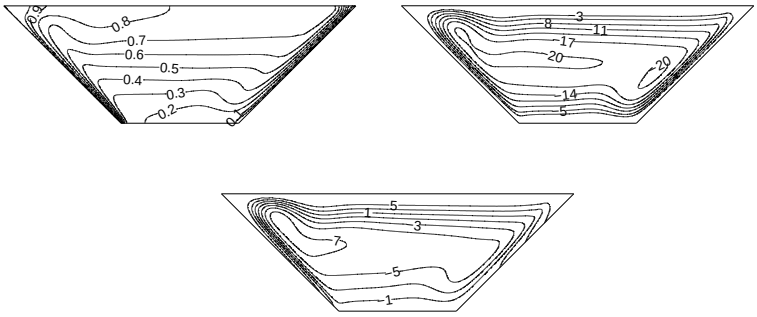

Figure 3: Temperature (left), stream function (right) and heatlines (bottom) for $Ra = 10^6$ and $Pr = 0.7$ with $\varphi = 45°$.

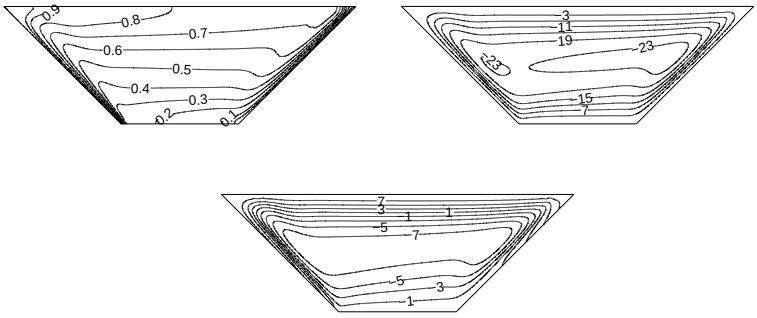

Figure 4: Temperature (left), stream function (right) and heatlines (bottom) for $Ra = 10^6$ and $Pr = 10$ with $\varphi = 45°$.

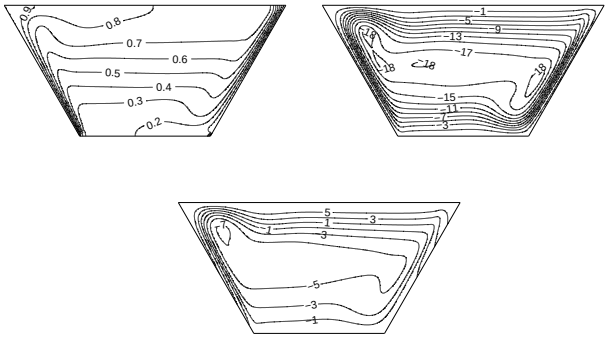

Figure 5: Temperature (left), stream function (right) and heatlines (bottom) for $Ra = 10^6$ and $Pr = 0.7$ with $\varphi = 30°$.

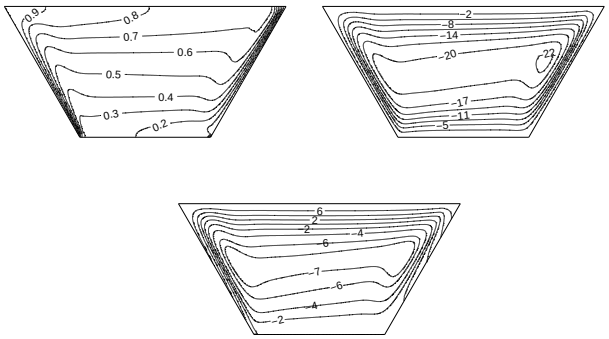

Figure 6: Temperature (left), stream function (right) and heatlines (bottom) for $Ra = 10^6$ and $Pr = 10$ with $\varphi = 30^\circ$.

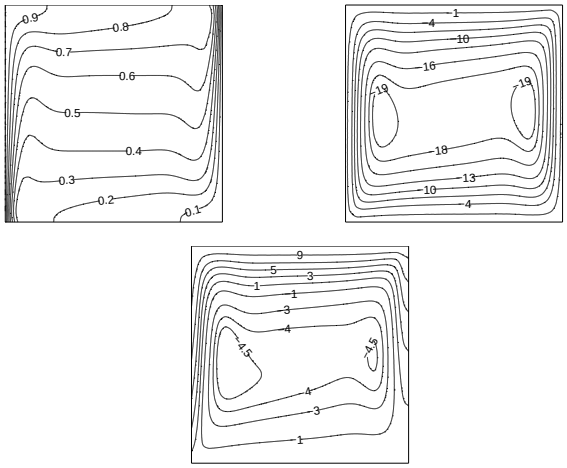

Figure 8: Temperature (left), stream function (right) and heatlines (bottom) for $Ra = 10^6$ and $Pr = 10$ with $\varphi = 0^\circ$.

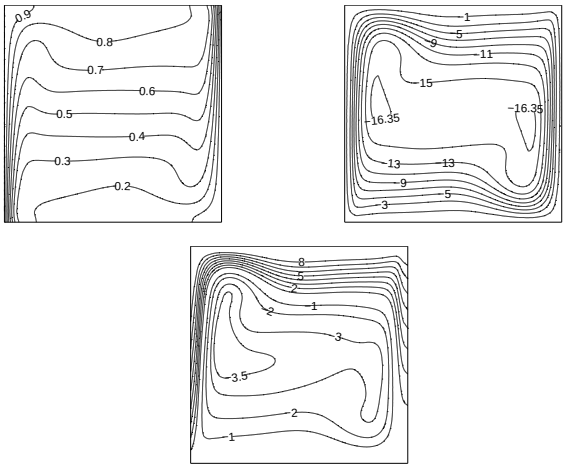

Figure 7: Temperature (left), stream function (right) and heatlines (bottom) for $Ra = 10^6$ and $Pr = 0.7$ with $\varphi = 0^\circ$.

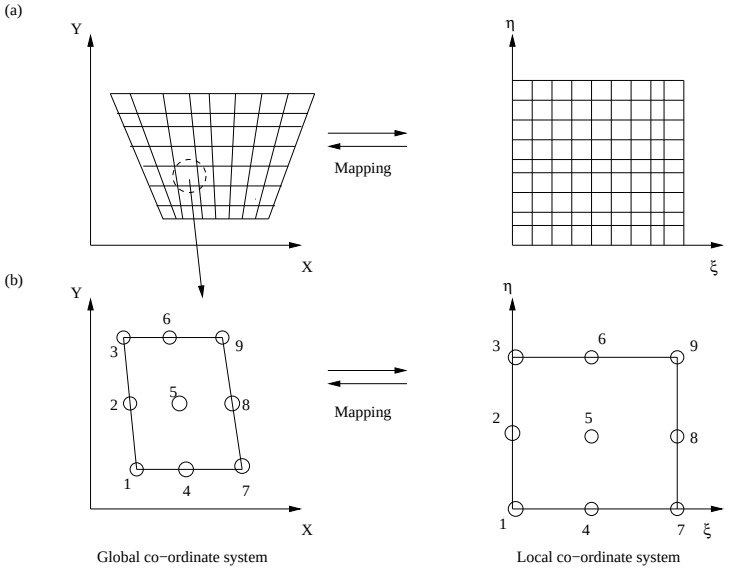

Figure 9: (a) The mapping of trapezoidal domain to a square domain in ξ-η coordinate system and (b) the mapping of an individual element to a single element in ξ-η coordinate system.